博 士 論 文

Histochemical assessment of accelerated bone remodeling and reduced mineralization in IL-6 deficient mice

（IL-6 欠損マウスにおける骨リモデリング促進と骨基質石灰化抑制の組織学的解析）

令和 3 年 3 月申請

北海道大学
大学院歯学研究科口腔医学専攻

森谷　康人

Histochemical assessment of accelerated bone remodeling and reduced mineralization in IL-6 deficient mice

Yasuhito Moritani

Oral and Maxillofacial Surgery, Graduate School of Dental Medicine, Hokkaido University, Sapporo, Japan

Running title: ***bone remodeling and mineralization in IL-6 deficiency***

§ **Address for correspondence to**

Yasuhito Moritani

Oral and Maxillofacial Surgery,

Graduate School of Dental Medicine,

Hokkaido University,

Kita-13, Nishi-7, Kita-Ku, Sapporo, Japan

Tel/Fax: +81-11-706-4283

E-mail: ymoritani0412@gmail.com

Abstract

We examined the femora of 8-week-old male, IL-6 deficient (IL-$6^{-/-}$) mice and their wild-type littermates by micro-CT analysis, immunohistochemistry, and real-time PCR to clarify the biological function of interleukin 6 (IL-6) in long bones. IL-$6^{-/-}$ femora showed an increased bone volume/tissue volume (BV/TV) but a reduced bone mineral density (BMD). Compared with the wild-type littermates, the tissue-nonspecific alkaline phosphatase (TNALPase) positive area/TV ratio and the gene expressions of *Runx2* and *Osterix* were elevated; in addition, in the IL-$6^{-/-}$ mice, the number of tartrate-resistant acid phosphatase (TRAP)-positive osteoclasts and the expression of *Rankl* (but not *Rank* and *Opg)* were increased. A considerable amount of unmineralized areas of bone matrix was observed using von Kossa staining in IL-$6^{-/-}$ femoral metaphyases but not in the wild-type counterparts. Thus, osteoblastic activities appeared to be facilitated by accelerated bone remodeling; however, bone mineralization seemed to be less active with abundant sclerostin-reactive osteocytes. Interestingly, in IL-$6^{-/-}$ femora, the gene expressions of *Cd206* were elevated, and many F4/80-positive macrophages/monocytes, as well as CD206 immunoreactive macrophages in the primary trabeculae, had migrated closer to the growth plate, where intense RANKL immunoreactivity was seen. Therefore, it is possible that, in an IL-6 deficient state, CD206-positive macrophages may differentiate into osteoclasts when in contact with RANKL-reactive osteoblastic cells. Taken together, these findings indicate that IL-6 deficiency causes accelerated bone remodeling and reduced bone mineralization induced by abundant sclerostin synthesis, indicating impaired bone remodeling and mineralization.

235 words

Key words: *IL-6, mineralization, CD206, osteoclast, sclerostin, RANKL,*

Introduction

Interleukin-6 (IL-6) is a member of the gp130 family, which is composed of IL-6, IL-11, oncostatin M, leukemia inhibitory factor, cardiotrophin-1, and novel neurotrophin-1/B-cell stimulatory factor-3; as a multifunctional protein, it is involved in the regulation of various normal biological functions in many tissues and organs (Heinrich et al., 1998; Senaldi et al. 1999). In bone, IL-6 is mainly expressed in osteoblastic cells but not in osteoclasts (Holt et al. 1996; Frost et al., 1998; Kozawa et al. 1998; Girasole et al. 1992; Miyaura et al., 1990). Both osteoblasts and osteoclasts are influenced by IL-6 family cytokines via signaling of glycoprotein 130 (gp130), a transmembrane signal transducer (Sims and Walsh 2010). For osteoclastogenesis and subsequent bone resorption, IL-6 reportedly affects osteoclasts and preosteoclasts, stimulating bone resorption of neonatal mouse calvaria in association with soluble receptor IL-6 (sIL-6R) (Palmqvist et al., 2002) and facilitates osteoclastogenesis in co-culture systems with mouse bone marrow cells and osteoblastic or stromal cells (Tamura et al., 1993). Thus, IL-6 seems to stimulate osteoclasts, and the biological function of IL-6 on osteoclastogenesis must be indirectly mediated by the receptor activator of nuclear factor kappa B ligand (RANKL) synthesis by osteoblasts (Yasuda et al., 1998). However, Gao et al. reported that gp130 and IL-6R are expressed in tartrate-resistant acid phosphatase (TRAP)-positive osteoclasts (Gao et al., 1998). They stated that IL-6 directly affected the enhancement of the resorbing activity in a dose-dependent manner, indicating the involvement of IL-6 in the formation and activation of osteoclasts. Nevertheless, other researchers have reported different results, pointing out that IL-6 down-regulates RANKL-induced osteoclastogenesis by diverting cells to the macrophage lineage (Duplomb et al., 2008; Yoshitake et al., 2008).

In addition to the participation of IL-6 in osteoclastogenesis, IL-6 affects osteoblasts by cooperating with sIL-6R (Ernst et al., 2004.); IL-6 binds to sIL-6R, promoting osteoblast differentiation by increasing the levels of alkaline phosphatase and osteocalcin through the mediation of gp130-linked signaling (Nishimura et al. 1998; Heymann and Rousselle 2000; Erices et al. 2002; Franchimont et al. 2005). Unlikely, others have documented that IL-6 negatively regulates osteoblast differentiation *in vitro* through the SHP2/MEK2 and SHP2/Akt2 pathways (Kaneshiro et al., 2014). Taken together, these reports imply that the true function of IL-6 on osteoblasts and

osteoclasts remains unclear (Heymann and Rousselle 2000; Franchimont et al. 2005).

The role of IL-6 in bone *in vivo* has been studied using various transgenic and gene-deficient mouse models; indeed, *in vitro* data have not been consistent and are often in conflict with those of *in vivo* experiments. Despite many reports of IL-6 functioning *in vitro* (Palmqvist et al., 2002, Tamura et al., 1993, Duplomb et al., 2008; Yoshitake et al., 2008, Nishimura et al. 1998; Heymann and Rousselle 2000; Erices et al. 2002; Franchimont et al. 2005, Kaneshiro et al., 2014), IL-6 deficient (IL-$6^{-/-}$) mice seem healthy and feature no specific bone phenotype (Kopf et al., 1994; Poli et al., 1994). Poli et al. reported that IL-$6^{-/-}$ female mice possess a normal amount of trabecular bone with no changes in osteoblast and osteoclast cell numbers, but the mice have a higher bone turnover rate than wild-type littermates (Poli et al., 1994). Interestingly, estrogen deficiency did not induce any change in bone mass or bone remodeling rates in the IL-$6^{-/-}$ mice. They stated that IL-6 plays an important role in the local regulation of bone turnover and therefore appears to be necessary for bone loss caused by estrogen deficiency. Although the biological function of IL-6 has been widely believed to mediate gp130 signaling when combined with sIL-6R, the number of osteoclasts in the $gp130^{-/-}$ fetuses of IL-$6^{-/-}$ mice were unexpectedly increased, in contrast to other findings (Kawasaki et al., 1997). In addition, de Benedetti et al. noted the retarded individual growth of mice and an osteopenic phenotype in IL-6 transgenic mice at 10 days after birth (de Benedetti et al., 2006); histological alterations in the cortical and trabecular bone, as well as uncoupling of bone formation from resorption, with decreased osteoblast and increased osteoclast numbers and activities, were observed. They also described that increased osteoclastogenesis and reduced osteoblast activity, secondary to reduced precursor proliferation and osteoblast function, were present. The mineral apposition rates were markedly affected, indicating the presence of defective ossification. It is interesting that the findings from $gp130^{-/-}$ fetuses and IL-6 transgenic mice are not consistent with the interpretation of IL-6 function gleaned from the histological findings in IL-$6^{-/-}$ mice, which seemingly presented with a normal amount of trabecular bone and with no changes in osteoblast and osteoclast cell numbers. Recently, we histologically examined bone remodeling influenced by IL-6 deficiency using a middle-aged (8–12 months) mouse model. IL-6 deficiency resulted in an abundance of TRAP-positive osteoclasts but delayed bone remodeling by significantly inhibiting the bone resorption activity of osteoclasts.

Because of the inconsistent and contradictory data of previous studies, the function of IL-6 on osteoblasts and osteoclasts remains unclear. It is, therefore, worthwhile to examine the bone histology in IL-$6^{-/-}$ mice. This study has aimed to evaluate the histological activities of osteoblasts and osteoclasts in the femora of young adult IL-$6^{-/-}$ mice.

Materials and methods

Animals and tissue preparation

Eight-week-old male IL-$6^{-/-}$ mice and wild-type littermates (n = 6 each, Jakson Laboratories, Bar Harbor, ME) were used in this study. The principles for care and research use of animals set by Hokkaido University were followed (research proposal approved under No. 20-0024). The mice were anesthetized with an intraperitoneal injection of a combination of anesthetic agents (0.3 mg/kg of medetomidine, 4.0 mg/kg of midazolam, and 5.0 mg/kg of butorphanol) and perfused with 4% paraformaldehyde diluted in 0.1 M cacodylate buffer (pH 7.4) through the left cardiac ventricle. The femora and tibiae were immediately removed and immersed with the same fixative for 18 hrs at 4 °C. Before decalcification, the left femora were soaked in 0.1 M cacodylate buffer prior to micro-CT analyses. The left femora and tibiae were decalcified with 10% ethylenediaminetetraacetic disodium salt (EDTA-Na_2) solution and 5% EDTA-Na_2 solution for light microscopic and electron microscopic observation, respectively (Hasegawa et al., 2013). The right femora were used for real-time PCR analysis, while the right tibiae were processed for epoxy resin embedding without decalcification. For light microscopy, the decalcified left femora were dehydrated in ascending alcohol solutions prior to paraffin embedding and sectioning. For transmission electron microscopy (TEM) observations, the decalcified left tibiae or undecalcified right tibiae were post-fixed with 1% osmium tetroxide with a 0.1 M cacodylate buffer for 4 hr at 4 °C, dehydrated in ascending acetone solutions, and embedded in epoxy resin (Epon 812, TAAB, Berkshire, UK). Ultrathin sections were prepared with an ultramicrotome and stained with uranyl acetate and lead citrate or left unstained for TEM examination (Hitachi H-7100 Hitachi Co. Ltd, Tokyo, Japan) at 80 kV (Hasegawa et al., 2011).

Micro-CT analysis

Micro-CT images were obtained from the femora of the wild-type and IL-$6^{-/-}$ mice with a micro-CT unit (tube voltage 90 kV, CosmoScan FX, Rigaku Corporation, Tokyo, Japan). CT analyzer software (CosmoScan Viewer, Rigaku Corporation, Tokyo, Japan) was used for image reconstruction per the guidelines described by Bouxsein et al. For the analysis of bone mineral density (BMD, mg/mm^3) and bone volume/tissue volume (BV/TV, %), the ROIs were defined as the articular surface of the

distal femoral epiphysis and a diaphyseal area 8 mm away from the articular surface with inclusion of the cortical plates. The BMD and BV/TV in the femora of the wild-type and IL-$6^{-/-}$ mice were analyzed using BMD Analysis software (Rigaku Corporation, Tokyo, Japan).

Immunohistochemistry for tissue-nonspecific alkaline phosphatase (TNALPase), osteopontin, type I collagen, sclerostin, cathepsin K, vacuolar-type ATPase (V-ATPase d 3 subunit), PKR, RANK, RANKL, F4/80, and CD206

For immunodetection using horseradish peroxidase (HRP)-conjugated secondary antibodies, all dewaxed paraffin sections were subjected to inhibition of the endogenous peroxidase activity by soaking in methanol containing 0.3% hydrogen peroxidase for 30 min and pretreatment with 1% bovine serum albumin (BSA; Serologicals Proteins Inc., Kankakee, IL) in PBS (1% BSA–PBS) for 30 min.

The subsequent incubation with the primary antibodies is described elsewhere (Hasegawa et al., 2019). In brief, for detection of tissue-nonspecific alkaline phosphatase (TNALPase), osteopontin, vacuolar-type ATPase (V-ATPase), PKR, and CD206, the dewaxed sections treated above were incubated with rabbit polyclonal antisera against TNALPase (Oda et al., 1999) diluted 1:300 with 1% BSA–PBS for 2 hr at room temperature (RT), rabbit anti-osteopontin antisera (Cosmo Bio, Co., Ltd., Tokyo, Japan) diluted 1:2000 for 2 hr at RT, rabbit polyclonal antisera against d3 subunits of vacuolar-type proton pump ATPase (Immuno-Biological Laboratories. Co., Ltd, Fujioka, Japan; kindly provided by Daiichi-Sankyo Co. Ltd., Tokyo Japan) diluted 1:100 with 1% BSA–PBS for 2 hr at RT, rabbit anti-PKR antibody (Abcam. plc., Cambridge, UK), and rabbit anti-CD206 antibody (Abcam. plc., Cambridge, UK), respectively. The sections thusly reacted with the primary antibodies were incubated with (HRP)-conjugated goat anti-rabbit IgG (DakoCytomation, Glostrup, Denmark) diluted 1:100 for 1 hr at RT. For the immunodetection of sclerostin, RANKL, and RANK, the dewaxed paraffin sections treated with hydrogen peroxidase and 1% BSA–PBS were incubated with goat anti-mouse sclerostin antibody (R&D Systems, Inc., Minneapolis, MN) diluted 1:100, goat anti-mouse RANKL antibody (R&D Systems, Inc.) diluted 1:100, and goat anti-mouse RANK antibody (R&D Systems, Inc.) diluted 1:100, respectively. Those treated sections were reacted with HRP-conjugated anti-goat IgG (American Qualex, San Clemente, CA) diluted 1:100 for 1 h at RT. For

cathepsin K immunohistochemistry, the sections were incubated with mouse anti-human cathepsin K (Daiichi Fine Chemical Co., Ltd., Takaoka, Japan) diluted 1:200 overnight and then incubated with HRP-conjugated anti-mouse IgG (Chemicon International Inc., Temecula, CA) diluted 1:100. For detection of F4/80, the dewaxed paraffin sections treated with hydrogen peroxidase and 1% BSA–PBS were incubated with rat anti-mouse F4/80 (Novus Biologicals, LLC., Centennial, CO) diluted 1:100 at RT for 2 hr and then reacted with HRP-conjugated anti-rat IgG (Zymed Laboratories Inc., South San Francisco, CA) diluted 1:100.

For visualizations of all immunoreactions using HRP-conjugated secondary antibodies, 3,3'-diaminobenzidine tetrahydrochloride (Dojindo Laboratories, Kumamoto, Japan) was employed as a substrate. All sections were counterstained with methyl green and observed under a light microscope (Eclipse E800, Nikon Instruments Inc., Tokyo, Japan).

As with the immunofluorescent detection of CD206, the sections were incubated with rabbit anti-CD206 antibody (Abcam. plc.) and then with Alexa488-conjugated donkey anti-goat IgG (Abcam. plc.) diluted 1:100 with 1% BSA-PBS. The sections were embedded using VECTASHIELD hard-set mounting medium with DAPI (Vector Laboratories, Inc. Burlingame, CA) and observed using a fluorescence microscope.

Enzyme histochemistry for tartrate-resistant acid phosphatase (TRAP)

Tartrate-resistant acid phosphatase (TRAP) was detected as previously described (Hasegawa et al., 2019); in short, slides were rinsed with PBS and incubated in a mixture of 2.5 mg of naphthol AS-BI phosphate (Sigma-Aldrich Co. LLC, St. Louis, MS), 18 mg of red-violet LB (Sigma) salt, and 100 mM L (+) tartaric acid (0.76 g, Nacalai Tesque, Inc., Kyoto, Japan) diluted in 30 mL of 0.1 M sodium acetate buffer (pH 5.0) for 15 min at 37 °C. Following immunostaining, TRAP detection was conducted as described above.

Von Kossa staining

Epoxy resin sections of the undecalcified specimens were incubated with an aqueous silver nitrate solution until black staining of the bone tissue was discernible under light microscopy (Hasegawa et al., 2019).

Quantification of TNALPase(+) area/TV and the numbers of TRAP-positive osteoclasts

An assumed boxed area (ROI: region of interest) with dimensions 800 μm (width) × 1000 μm (length) located directly below the femoral growth plate was used to assess the TNALPase-reactive area/TV ratio and the number of TRAP-positive osteoclasts. These indices were determined using Image-Pro Plus 6.2 (Media Cybernetics, Inc., Bethesda MD).

Real-time PCR for the expression of Runx2, Osterix, Sost, Rankl, Rank, Opg, Cd11c, Cd206, Tnfα, and Gapdh in the femora of the wild-type and IL-6$^{-/-}$ littermates

To evaluate the mRNAs encoding *Runx2, Osterix, Sost, Rankl, Rank, Opg, Cd11c, Cd206, Tnfα, and Gapdh*, total RNA was extracted from the right femora of the wild-type mice and IL-6$^{-/-}$ littermates as previously reported (Hasegawa et al., 2013). In brief, the femora were immediately frozen in liquid nitrogen and cracked into small pieces. The cracked femora were homogenized in 10 mL of TRIzol reagent (Life Technologies Co., Carlsbad, CA) per 1 g of tissue to extract the total RNA. The obtained RNA pellet was washed with 1 mL of 75% ethanol, air-dried briefly, and dissolved in DEPC-treated water. First-strand cDNA was synthesized from 2 μg of total RNA using a SuperScript VlLO cDNA Synthesis Kit (Life Technologies).

Real-time PCR assays were performed using Taqman probes (Applied Biosystems) to determine the gene expressions of *Runx2* (Mm00501584_m1), *Osterix* (Mm04209856_m1), *Sost* (Mm00470479_m1), *Rankl* (Mm00441906_m1), *Rank* (Mm00437132_m1), *Opg* (Mm00435454_m1), *Cd11c* (Mm00498701_m1), *Cd206* (Mm01329362_m1), and *Tnfα* (Mm00443258_m1). Gene expression was measured using the StepOne Real-Time PCR System (Applied Biosystems), and the expression levels were normalized to *Gapdh* (Mm99999915_g1) using the 2ΔΔCt method.

Statistical analysis

Statistical analyses for the indices of the gene expression (*Runx2, Osterix, Sost, Rankl, Rank, Opg, Cd11c, Cd206,* and *Tnfα*; standardized by *Gapdh* expression), BMD, BV/TV, TNALPase(+) area/TV, and the numbers of TRAP-positive osteoclasts were assessed using Student's t-test. All values are

presented as mean ± standard deviation. Values of $p < 0.05$ were considered significant.

Results

Reduced bone mineral density but increased bone volume in IL-6$^{-/-}$ femoral metaphyses

Micro CT analysis revealed the similar structure of femoral metaphyses of IL-6$^{-/-}$ mice and wild-type littermates **(Fig. 1A, B)**. However, when compared with the wild-type femora, IL-6$^{-/-}$ femora showed a reduced BMD (1422.2 $\pm$ 10.8 mg/mm^3 wild-type vs. 1220.4 $\pm$ 23.1 mg/mm^3 IL-6$^{-/-}$, $p<0.01$) but an increased BV/TV (66.8 $\pm$ 0.9 % wild-type vs. 71.7 $\pm$ 0.6 % IL-6$^{-/-}$, $p<0.05$) **(Fig. 1C, D)**. Histologically, there seemed to be increased metaphyseal trabeculae in IL-6$^{-/-}$ femora, compared with the wild-type femora **(Fig. 1E, F)**. When examined using von Kossa staining to visualize mineralized bone matrix **(Fig. 2A-D)**, the IL-6$^{-/-}$ metaphyseal trabeculae showed thick layers of unmineralized bone matrix **(Fig. 2B, D)**, compared with wild-type trabeculae **(Fig. 2A, C)**. This indicates that, despite the increased bone volume, the attenuated BMD seems to be, at least in part, due to a huge area of unmineralized bone matrix in the IL-6$^{-/-}$ metaphyseal trabeculae. TEM observation revealed the similar ultrastructure of mature osteoblasts in the metaphyses of the wild-type and IL-6$^{-/-}$ femora **(Fig. 2E, F)**.

Increased TNALPase(+) area/TV and elevated expression of Runx2, Osterix, and Sost in IL-6$^{-/-}$ femoral metaphyses

Intense TNALPase immunoreactivity was broadly localized in the metaphyses of IL-6$^{-/-}$ femora, rather than the wild-type femora **(Fig. 3A, B)**. Consistently, the index of TNALPase(+) area/TV was markedly increased in the ROI of the IL-6$^{-/-}$ femora, compared with the wild-type specimens **(Fig. 3C)**. In addition, real-time PCR revealed elevated expression of *Runx2* and *Osterix* in the IL-6$^{-/-}$ femora when compared with the wild-type specimens **(Fig. 3D, E)**. The statistical analyses supported the significantly elevated indices of *Runx2* and *Osterix*: 0.97 $\pm$ 0.17 in wild-type mice vs. 2.93 $\pm$ 0.25 in IL-6$^{-/-}$ mice ($p<0.01$) and 1.05 $\pm$ 0.17 in wild-type mice vs. 2.36 $\pm$ 0.21 in IL-6$^{-/-}$ mice ($p<0.05$), respectively **(Fig. 3C-E)**. Despite the increased expression of *Runx2* and *Osterix* in IL-6$^{-/-}$ femora, sclerostin immunoreactive osteocytes were abundant in the IL-6$^{-/-}$ metaphysis relative to the wild-type counterparts **(Fig. 4A-F)**. Consistent with sclerostin immunolocalization, real-time PCR showed markedly increased expression of the *Sost* gene encoding sclerostin in IL-6$^{-/-}$ mice, when

compared with the wild-type (2.69 ± 1.72 wild-type vs. 13.70 + 3.20 IL-6$^{-/-}$, *p<0.05*) **(Fig. 4G)**.

Increased numbers of TRAP-positive osteoclasts and enhanced expression of cathepsin K and RANKL in IL-6$^{-/-}$ femoral metaphyses

TRAP-positive osteoclasts were abundantly localized in IL-6$^{-/-}$ femoral metaphyses, unlike those in the wild-type metaphyses **(Fig. 5A, B)**. Consistently, cathepsin K-reactive osteoclasts were increased in IL-6$^{-/-}$ metaphyses compared with the wild-type specimens **(Fig. 5C, D)**. There were many osteopontin-positive lines on and inside the IL-6$^{-/-}$ metaphyseal trabeculae, while an even distribution of osteopontin could be seen throughout the wild-type trabeculae **(Fig. 5E, G)**. In contrast, type I collagen was uniformly localized in the metaphyseal trabeculae of both the wild-type and IL-6$^{-/-}$ femora **(Fig. 5F-H)**. The numbers of TRAP-positive osteoclasts in the ROI was significantly increased in IL-6$^{-/-}$ femoral metaphyses (66.20 ± 2.52) compared with the wild-type counterpart (35.33 ± 0.62, *p<0.001*) **(Fig. 5I)**. Additionally, real-time PCR revealed a slightly but not significantly increased expression of *Cathepsin K* in IL-6$^{-/-}$ femora compared with the wild-type counterparts **(Fig. 5J)**.

Moreover, we examined the immunolocalization of the d3 subunits of V-ATPase, PKR, RANK, and RANKL. The immunoreactivities of V-ATPase, PKR, and RANK were observed in osteoclasts in both the wild-type and IL-6$^{-/-}$ femoral metaphyses without any apparent differences between the two groups **(Fig. 6A-F)**. In contrast, there was relatively intense RANKL immunoreactivity in IL-6$^{-/-}$ osteoblastic cells compared with the wild-type osteoblasts **(See Fig. 6G, H)**. Consistent with the immunodetection of these molecules, real-time PCR showed an increased expression of *Rankl* (but not *Rank* or *Opg*) in the IL-6$^{-/-}$ femora relative to the wild-type femora **(Fig. 6I-K)**.

Immunolocalization of F4/80 monocytes/macrophages and elevated gene expression of CD11c, CD206, and Tnfα in IL-6$^{-/-}$ femora

Although the number of F4/80-positive cells were not significantly different between the wild-type femora and IL-6$^{-/-}$ specimens, F4/80-positive cells in the primary metaphyseal trabeculae migrated closer to the chondro-osseous junction of the growth plate cartilage when compared with those in the

wild-type counterparts **(Fig. 7A-D)**. Likewise, many CD206-immunoreactive cells were observed in the intertrabecular region of the primary trabeculae in the IL-$6^{-/-}$ femora but not the wild-type specimens **(Fig. 7E, F)**. Real-time PCR revealed enhanced gene expressions of *Cd11c*, *Cd206,* and *Tnfα* in the IL-$6^{-/-}$ femora when compared with the wild-type specimens **(Fig. 7G-I)**; the ratios of *Cd11c*, *Cd206,* and *Tnfα* standardized with the gene expression of *Gapdh* were as follows: 0.84 $\pm$ 0.16 control vs. 2.26 $\pm$ 0.19 IL-$6^{-/-}$ for *Cd11c* ($p<0.01$), 0.86 $\pm$ 0.14 control vs. 5.88 $\pm$ 0.12 IL-$6^{-/-}$ for *Cd206* ($p<0.01$), and 0.58 $\pm$ 0.21 control vs. 5.42 $\pm$ 0.35 IL-$6^{-/-}$ for *Tnfα* ($p<0.01$).

Discussion

Here, we have shown that in IL-6$^{-/-}$ femora, 1) despite the increased BV/TV ratio, the BMD was significantly reduced; 2) using von Kossa staining, a considerable amount of unmineralized areas were present in the bone matrix with an abundance of sclerostin-reactive osteocytes; 3) the TNALPase(+) area/TV ratio and the gene expressions of *Runx2* and *Osterix* were elevated; 4) the numbers of TRAP-positive osteoclasts and the expression of *Rankl* were increased with no change of *Rank* and *Opg*; and 5) the gene expressions of *Cd11c* and *Cd206* were elevated, and many F4/80-positive macrophages/monocytes and CD206 immunoreactive macrophages were localized in the primary trabeculae close to the growth plate.

These findings may suggest that bone remodeling is promoted by cell coupling between osteoblasts and osteoclasts, which can be histologically evidenced by the many osteopontin-immunopositive lines indicative of cement lines (the boundary between new and old bone in the metaphyseal trabeculae of IL-6$^{-/-}$ femoral metaphyses). BMD and von Kossa staining may reflect the amount of unmineralized bone matrix, while decalcified paraffin sections reveal the histological appearance of bone even though they were not well mineralized. Previous reports have been inconsistent and contradictory in the elucidation of IL-6 function (Palmqvist et al., 2002, Tamura et al., 1993, Duplomb et al., 2008; Yoshitake et al., 2008, Nishimura et al. 1998; Heymann and Rousselle 2000; Erices et al. 2002; Franchimont et al. 2005, Kaneshiro et al., 2014); however, our study has shown that the observed IL-6$^{-/-}$ bone volume can vary when examined using different observation methods, such as light microscopy of decalcified sections or micro-CT analysis of undecalcified bone.

It is interesting that even though osteoblastic activities were facilitated, as indicated by TNALPase(+) area/TV and expressions of *Runx2* and *Osterix*, the expression of the *Sost* gene encoding sclerostin (Winkler et al., 2003) was elevated 5.1 times higher than that of the wild-type counterpart when examined by real-time PCR. Consistent with our observation, Yang et al. have reported that callus mineralization was delayed during fracture healing in interleukin-6 knockout mice (Yang et al., 2007). There might be a direct influence of IL-6 in blocking the synthesis of sclerostin. However, it has been reported that TNFα also mediates the stimulation of sclerostin expression under an estrogen-deficient condition (Kim et al., 2012). Thus, it is likely that IL-6 deficiency or the

combined effect of IL-6 deficiency and elevated TNFα would stimulate sclerostin synthesis in femoral metaphyses. A mutation of the *Sost* gene encoding sclerostin was discovered in patients with osteosclerosis who did not have increases in bone volume (Kim et al., 2008; Piters et al., 2010). Therefore, it seems reasonable that an increased sclerostin immunoreactivity and elevated *Sost* expression would result in the lack of mineralized bone matrix of the IL-$6^{-/-}$ femora, as shown in **Figure 2**. Taken together, it seems likely that, in an IL-6 deficient state, bone mineralization would be attenuated because of increased sclerostin, even though osteoblastic activities were facilitated by coupling with an increased population of TRAP-positive osteoclasts.

It is interesting that not only were the osteoclasts changed, but subpopulations of macrophages were as well, as shown in **Figure 7**. Many reports have indicated that CD206 is a hallmark of M2 macrophages (Kambara et al., 2017), while CD11c is a maker of M1 macrophages (Lumeng et al., 2007; Fujisaka et al., 2009). Classical activated or "M1" macrophages secrete high amounts of inflammatory mediators while the alternatively activated "M2" macrophages are low cytokine producers (Fuentes et al., 2010). A recent report documented that, in bone, M2 macrophages could differentiate into osteoclasts in the presence of RANKL without pretreatment of estrogen (Dou et al., 2018). In our observation, CD206-positive M2 macrophages were abundant in the IL-$6^{-/-}$ metaphyses, consistent with the elevated expression of CD206. In addition, CD206-positive macrophages and F4/80-immunoreactive monocytes/macrophages in the primary trabeculae were observed close to the growth plate cartilage, where osteoblasts displayed an intense RANKL immunoreactivity in the IL-$6^{-/-}$ femora, as shown in **Figure 6**. Taken together, it seems possible that, in an IL-6 deficient state, M1/M2 macrophages would increase their numbers, and CD206-positive M2 macrophages may differentiate into osteoclasts when in contact with RANKL-reactive osteoblastic cells.

Conclusion

This study revealed the presence of increased trabecular volume, reduced bone mineralization, accelerated bone remodeling by osteoclasts and osteoblasts, and increased macrophage subpopulations in the IL-$6^{-/-}$ femora. It is of interest that even though osteoblastic activities appeared to be facilitated because of accelerated bone remodeling, sclerostin-reactive osteocytes were abundant. Taken together, these findings indicate that IL-6 deficiency causes accelerated bone remodeling and reduced bone mineralization, presumably induced by abundant sclerostin synthesis.

Conflict of interest

No potential conflicts of interest exist.

References

1. Bouxsein ML, Boyd SK, Christiansen BA, Guldberg RE, Jepsen KJ, Müller R (2010) Guidelines for assessment of bone microstructure in rodents using micro-computed tomography. J Bone Miner Res. 25(7):1468 –1486.

2. Dou C, Ding N, Zhao C, Hou T, Kang F, Cao Z, Liu C, Bai Y, Dai Q, Ma Q, Luo F, Xu J, Dong S (2018) Estrogen deficiency-mediated M2 macrophage osteoclastogenesis contributes to M1/M2 ratio alteration in ovariectomized osteoporotic mice. J Bone Miner Res. 33(5):899–908.

3. Duplomb L, Baud'huin M, Charrier C, Berreur M, Trichet V, Blanchard F, Heymann D. (2008) Interleukin-6 inhibits receptor activator of nuclear factor kappaB ligand-induced osteoclastogenesis by diverting cells into the macrophage lineage: key role of Serine727 phosphorylation of signal transducer and activator of transcription 3. Endocrinology. 149(7):3688–3697.

4. Erices A, Conget P, Rojas C, Minguell JJ. (2002) Gp130 activation by soluble interleukin-6 receptor/interleukin-6 enhances osteoblastic differentiation of human bone marrow-derived mesenchymal stem cells. Exp Cell Res. 280(1): 24–32.

5. Ernst M, Jenkins BJ. (2004) Acquiring signalling specificity from the cytokine receptor gp130. Trends Genet 20: 23–32.

6. De Benedetti F, Rucci N, Fattore AD, Peruzzi B, Paro R, Longo M, Vivarelli M, Muratori F, Berni S, Ballanti P, Ferrari S, Teti A. (2006) Impaired skeletal development in interleukin-6–transgenic mice: A model for the impact of chronic inflammation on the growing skeletal system. Arthritis Rheum 54(11): 3551–3563

7. Franchimont N, Wertz S, Malaise M. (2005) Interleukin-6: An osteotropic factor influencing bone formation? Bone. 37(5): 601–606.

8. Frost A, Jonsson KB, Brandstrom H, Ohlsson C, Ljunghall S, Ljunggren O. (1998) Interleukin-13 inhibits cell proliferation and stimulates interleukin-6 formation in isolated human osteoblasts. J Clin Endocrinol Metab 83:3285–3289.

9. Fuentes L, Roszer T, Ricote M. (2010) Inflammatory mediators and insulin resistance in obesity: role of nuclear receptor signaling in macrophages. Mediators Inflamm. 2010: 219583. doi: 10.1155/2010/219583.

10. Fujisaka S, Usui I, Bukhari A, Ikutani M, Oya T, Kanatani Y, Tsuneyama K, Nagai Y, Takatsu K, Urakaze M, Kobayashi M, Tobe K. (2009) Regulatory mechanisms for adipose tissue M1 and M2 macrophages in diet-induced obese mice. Diabetes 58(11): 2574–2582.

11. Gao Y, Morita I, Maruo N, Kubota T, Murota S, Aso T. (1998) Expression of IL-6 receptor and GP130 in mouse bone marrow cells during osteoclast differentiation. Bone 22: 487–493.

12. Girasole G, Jilka RL, Passeri G, Boswell S, Boder G, Williams DC, Manolagas SC (1992) 17 beta-estradiol inhibits interleukin-6 production by bone marrow-derived stromal cells and osteoblasts in vitro: a potential mechanism for the antiosteoporotic effect of estrogens. J Clin Invest 89: 883–891.

13. Hasegawa T, Amizuka N, Yamada T, Liu Z, Miyamoto Y, Yamamoto T, Sasaki M, Hongo H, Suzuki R, Freitas PHL, Yamamoto T, Oda K, Li M. (2013) Sclerostin is differently immunolocalized in metaphyseal trabecules and cortical bones of mouse tibiae. Biomed Res. 34(3): 153–159.

14. Hasegawa T., Li M., Hara K., Sasaki M., Tabata C., Freitas PHL., Hongo H., Suzuki R., Kobayashi M., Inoue K., Yamamoto T., Oohata N., Oda K., Akiyama Y., Amizuka N. (2011) Morphological assessment of bone mineralization in tibial metaphyses of ascorbic acid-deficient ODS rats. Biomed Res. 32(4): 259–269.

15. Hasegawa T., Miyamoto Y., Abe M., Qiu Z., Yamamoto T., Yimin, Yoshida T., Yoshino H., Hongo H., Yokoyama A., Sasaki M., Kuroshima S., Hara K., Kobayashi M., Akiyama Y., Maeda T., Freitas PHL., Li M., Amizuka N. (2019) Histochemical examination on principal collagen fibers in periodontal ligaments of ascorbic acid-deficient ODS-od/od rats. Microscopy. 68(5): 349–358.

16. Hasegawa T, Yamamoto T, Sakai S, Miyamoto Y, Hongo H, Qiu Z, Abe M, Takeda S, Oda K, Freitas PHL, Li M, Endo K, Amizuka N. (2019) Histological effects of the combined administration of eldecalcitol and a parathyroid hormone in the metaphyseal trabeculae of ovariectomized rats. J Histochem Cytochem. 67(3): 169-184.

17. Hasegawa T. (2018) Ultrastructure and biological function of matrix vesicles in bone mineralization. Histochem Cell Biol. 149(4): 289–304.

18. Heinrich PC, Behrmann I, Muller-Newen G, Schaper F, Graeve L. (1998) Interleukin-6-type cytokine signalling through the gp130/Jak/STAT pathway. Biochem J 334(Pt 2):297–314

19. Heymann D, Rousselle AV. (2000) Gp130 Cytokine family and bone cells. Cytokine 12(10):1455–1468.

20. Holt I, Davie MW, Marshall MJ. (1996) Osteoclasts are not the major source of interleukin-6 in mouse parietal bones. Bone 18: 221–226

21. Kambara K, Ohashi W, Tomita K, Takashina M, Fujisaka S, Hayashi R, Mori H, Tobe K, Hattori Y. (2015) In vivo depletion of CD206+ M2 macrophages exaggerates lung injury in endotoxemic mice. Am J Pathol 185: 162–171.

22. Kaneshiro S, Ebina K, Shi K, Higuchi C, Hirao M, Okamoto M, Koizumi K, Morimoto T, Yoshikawa H, Hashimoto J. (2014) IL-6 negatively regulates osteoblast differentiation through the SHP2/MEK2 and SHP2/Akt2 pathways in vitro. J Bone Miner Metab. 32(4): 378–392.

23. Kawasaki K, Gao YH, Yokose S, Kaji Y, Nakamura T, Suda T, Yoshida K, Taga T, Kishimoto T, Kataoka H, Yuasa T, Norimatsu H, Yamaguchi A. (1997) Osteoclats are present in gp130-deficient mice. Endocrinology 138: 4959–4965.

24. Kim BJ, Bae SJ, Lee SY, Lee YS, Baek JE, Park SY, Lee SH, Koh JM, Kim GS. (2012) TNF-α mediates the stimulation of sclerostin expression in an estrogen-deficient condition. Biochem Biophys Res Commun. 424(1): 170–175.

25. Kim CA, Honjo R, Bertola D, Albano L, Oliveira L, Jales S, Siqueira J, Castilho A, Balemans W, Piters E, Jennes K, Van Hul W. (2008) A known SOST gene mutation causes sclerosteosis in a familial and an isolated case from Brazilian origin. Genet Test. 12(4):475–479.

26. Kopf M, Baumann H, Freer G, Freudenberg M, Lamers M, Kishimoto T, Zinkernagel R, Bluethmann H, Köhler G. (1994) Impaired immune and acute-phase responses in interleukin-6-deficient mice. Nature 368: 339–342.

27. Kozawa O, Tokuda H, Kaida T, Matsuno H, Uematsu T. (1998) Retinoic acid suppresses interleukin-6 synthesis induced by prostaglandins in osteoblasts. Prostaglandins Leukop Essent Fatty Acids 58: 215–219.

28. Lumeng CN, Bodzin JL, Saltiel AR. (2007) Obesity induces a phenotypic switch in adipose tissue macrophage polarization. J Clin Invest 117:175–184;

29. Miyaura C, Jin CH, Akatsu T, Abe E, Nakamura Y, Yamaguchi A, Yoshiki S, Matsuda T, Hirano T, Kishimoto T, Suda T. (1990) Il-6 produced by osteoblasts and induces bone resorption. J Immunol 145: 3297–3303.

30. Nawaz A, Aminuddin A, Kado T, Takikawa A, Yamamoto S, Tsuneyama K, Igarashi Y, Ikutani M, Nishida Y, Nagai Y, Takatsu K, Imura J, Sasahara M, Okazaki Y, Ueki K, Okamura T, Tokuyama K, Ando A, Matsumoto M, Mori H, Nakagawa T, Kobayashi N, Saeki K, Usui I, Fujisaka S, Tobe K. (2017) CD206(+) M2-like macrophages regulate systemic glucose metabolism by inhibiting proliferation of adipocyte progenitors. Nat Commun 8: 286–303.

31. Nishimura R, Moriyama K, Yasukawa K, Mundy GR, Yoneda T. (1998) Combination of interleukin-6 and soluble interleukin-6 receptors induces differentiation and activation of JAK-STAT and MAP kinase pathways in MG-63 human osteoblastic cells. J Bone Miner Res. 13(5): 777–785.

32. Palmqvist P, Persson E, Conaway HH, Lerner UH. (2002) IL-6, leukemia inhibitory factor, and oncostatin M stimulate bone resorption and regulate the expression of receptor activator of NF-κB ligand, osteoprotegerin, and receptor activator of NF-κB in mouse calvariae. J Immunol 169: 3353–3362

33. Piters E, Culha C, Moester M, Van Bezooijen R, Adriaensen D, Mueller T, Weidauer S, Jennes K, de Freitas F, Löwik C, Timmermans JP, Van Hul W, Papapoulos S. (2010) First missense mutation in the SOST gene causing sclerosteosis by loss of sclerostin function. Hum Mutat. 31(7): E1526–1543.

34. Poli V, Balena R, Fattori E, Markatos A, Yamamoto M, Tanaka H, Ciliberto G, Rodan GA, Costantini F. (1994) Interleukin-6 deficient mice are protected from bone loss caused by estrogen depletion. EMBO J. 13(5):1189–1196.

35. Senaldi G, Varnum BC, Sarmiento U, Starnes C, Lile J, Scully S, Guo J, Elliott G, McNinch J, Shaklee CL, Freeman D, Manu F, Simonet WS, Boone T, Chang MS. (1999) Novel neurotrophin-1/B cell-stimulating factor-3: a cytokine of the IL-6 family. Proc Natl Acad Sci USA 96:11458–11463

36. Sims NA, Walsh NC. (2010) GP130 cytokines and bone remodelling in health and disease. BMB Rep. 43(8): 513–523.

37. Stewart AJ, Leong DTK, Farquharson C. (2018) PLA 2 and ENPP6 may act in concert to generate phosphocholine from the matrix vesicle membrane during skeletal mineralization. FASEB J. 32(1): 20–25.

38. Tamura T, Udagawa N, Takahashi N, Miyaura C, Tanaka S, Yamada Y, Koishihara Y, Ohsugi Y,

Kumaki K, Taga T, Kishimoto T, Suda T. (1993) Soluble interleukin-6 receptor triggers osteoclast formation by interleukin 6. Proc Natl Acad Sci USA 90:11924–11928

39. Winkler DG, Sutherland MK, Geoghegan JC, Yu C, Hayes T, Skonier JE, Shpektor D, Jonas M, Kovacevich BR, Staehling-Hampton K, Appleby M, Brunkow ME, Latham JA. (2003) Osteocyte control of bone formation via sclerostin, a novel BMP antagonist. EMBO J. 22(23): 6267–6276.

40. Yang X, Ricciardi BF, Hernandez-Soria A, Shi Y, Pleshko Camacho N, Bostrom MP. (2007) Callus mineralization and maturation are delayed during fracture healing in interleukin-6 knockout mice. Bone. 41(6): 928–936.

41. Yasuda H, Shima N, Nakagawa N, Yamaguchi K, Kinosaki M, Mochizuki S, Tomoyasu A, Yano K, Goto M, Murakami A, Tsuda E, Morinaga T, Higashio K, Udagawa N, Takahashi N, Suda T. (1998) Osteoclast differentiation factor is a ligand for osteoprotegerin/osteoclastogenesis-inhibitory factor and is identical to TRANCE/RANKL. Proc Natl Acad Sci USA. 95(7): 3597–3602.

42. Yoshitake F, Itoh S, Narita H, Ishihara K, Ebisu S. (2008) Interleukin-6 directly inhibits osteoclast differentiation by suppressing receptor activator of NF-kappa B signaling pathways. J Biol Chem. 283(17):11535–11540.

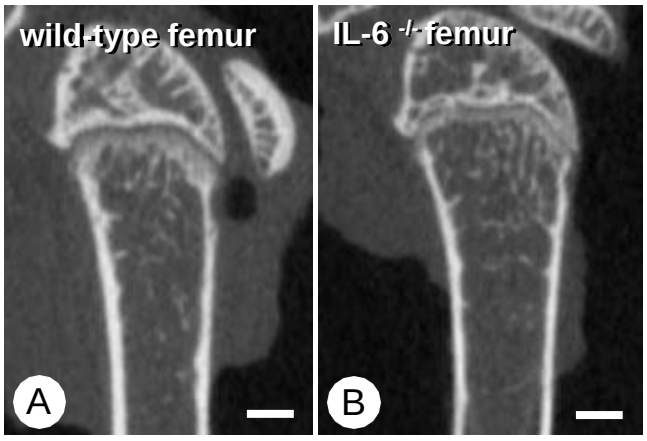
wild-type femur
IL-6 -/- femur
A
B

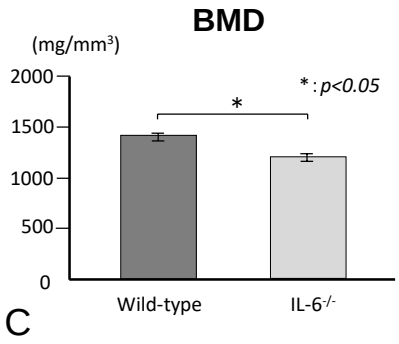
BMD
(mg/mm³)
2000
1500
1000
500
0
* : p<0.05
*
Wild-type
IL-6-/-
C

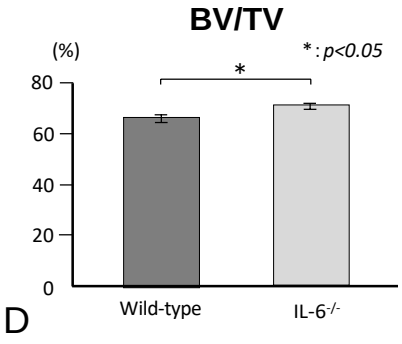
BV/TV
(%)
80
60
40
20
0
* : p<0.05
*
Wild-type
IL-6-/-
D

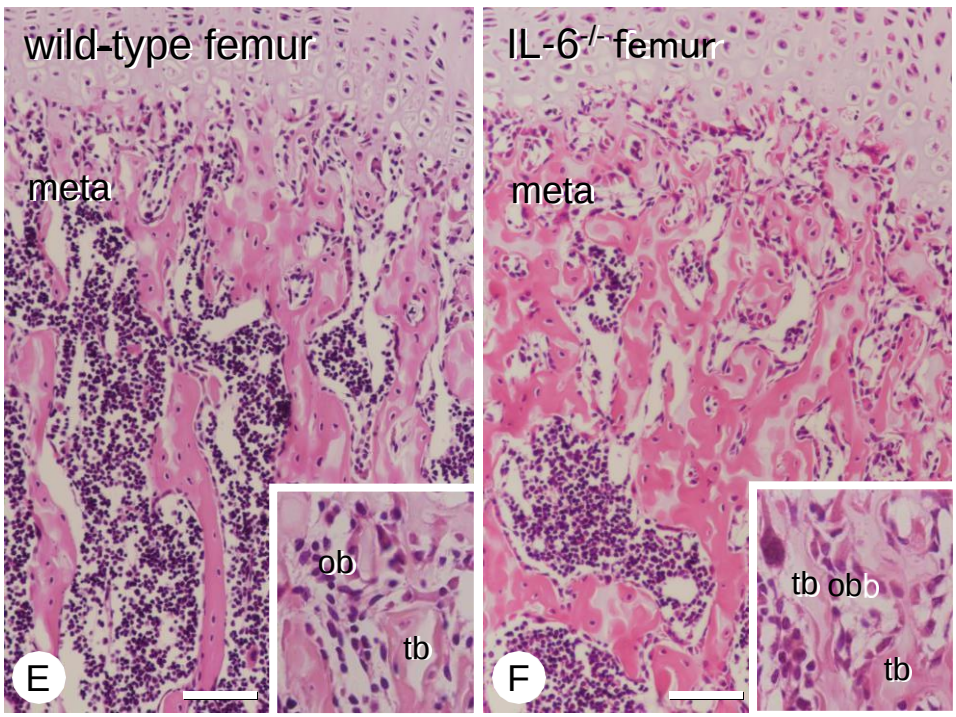
wild-type femur
meta
ob
tb
E
IL-6-/- femur
meta
tb ob
tb
F

Fig. 1

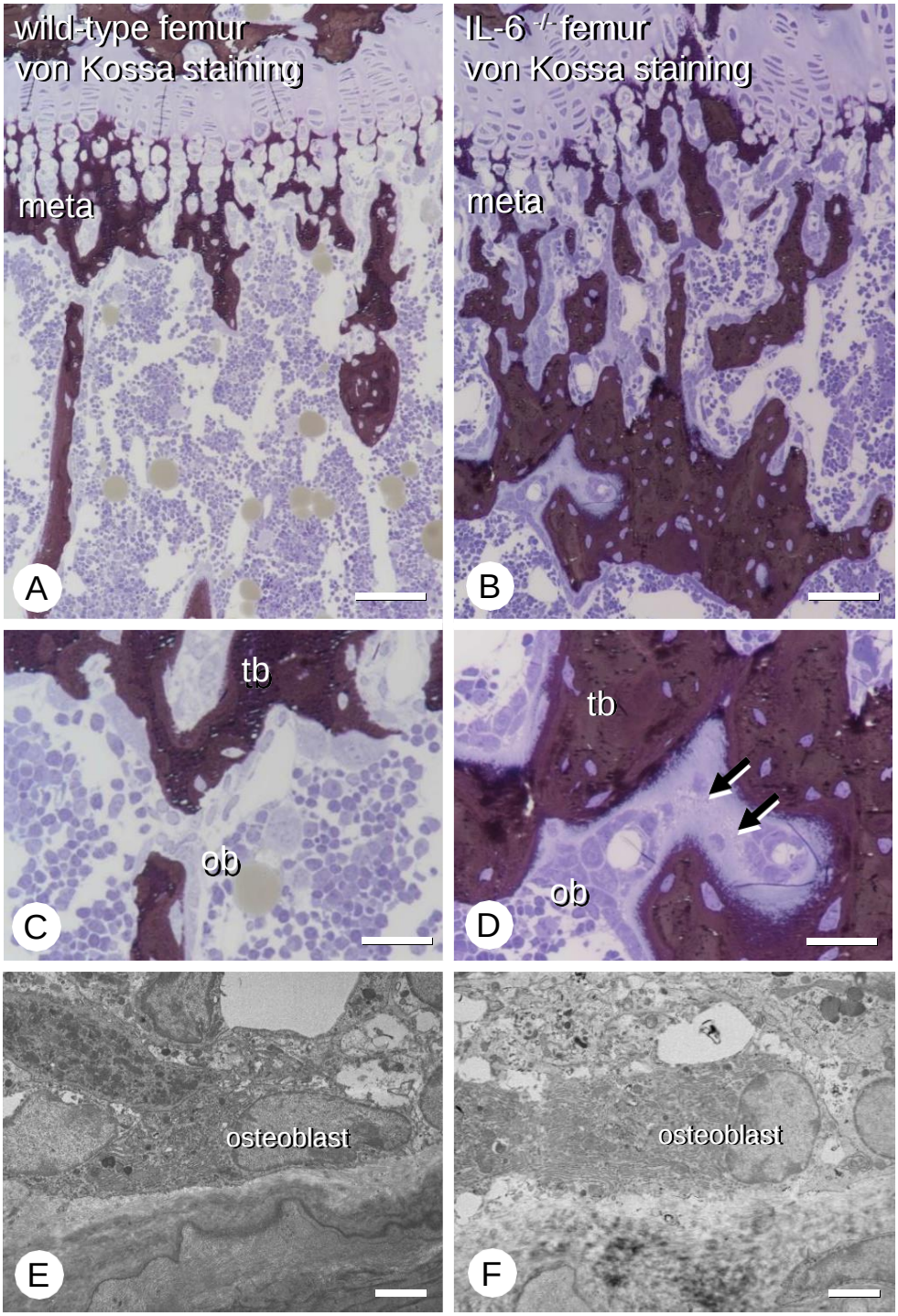
wild-type femur
von Kossa staining
meta
A
IL-6 -/- femur
von Kossa staining
meta
B
tb
ob
C
tb
ob
D
osteoblast
E
osteoblast
F

Fig. 2

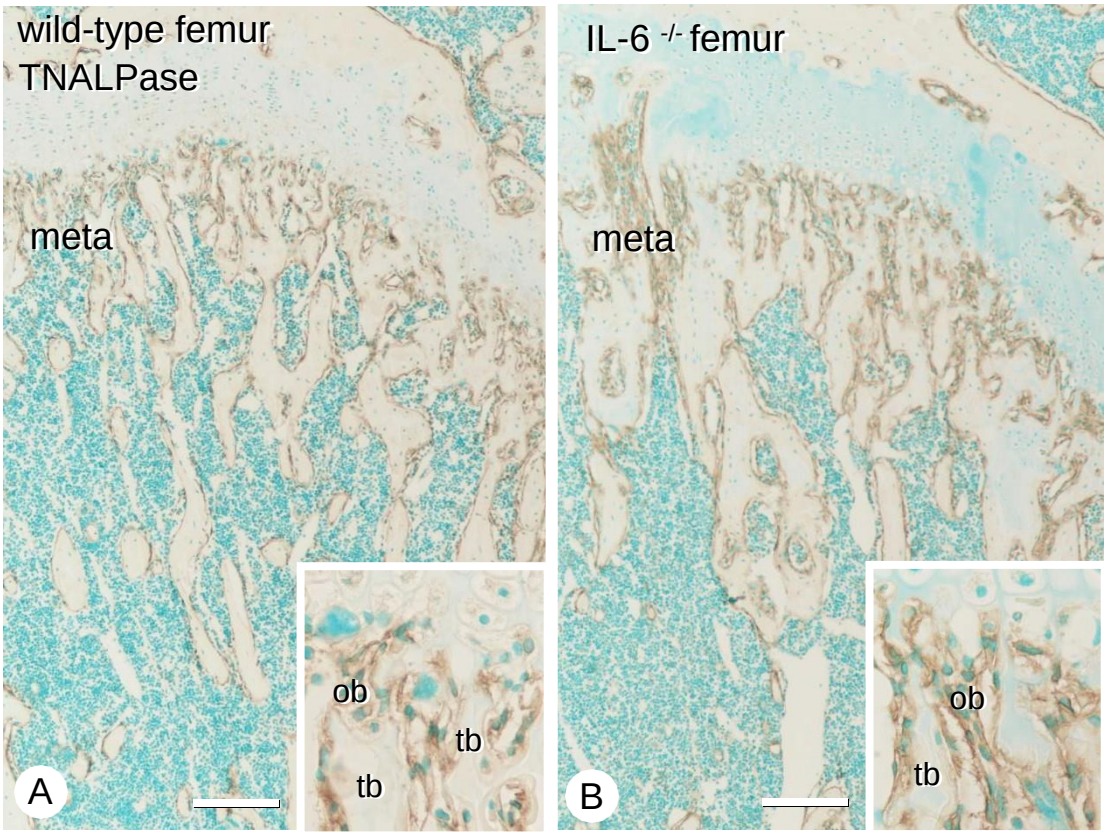
wild-type femur
TNALPase
meta
ob
tb
tb
A
IL-6 -/- femur
meta
ob
tb
B

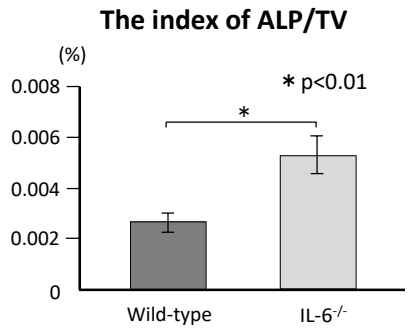
The index of ALP/TV
(%)
0.008
0.006
0.004
0.002
0
* p<0.01
*
Wild-type
IL-6-/-

C

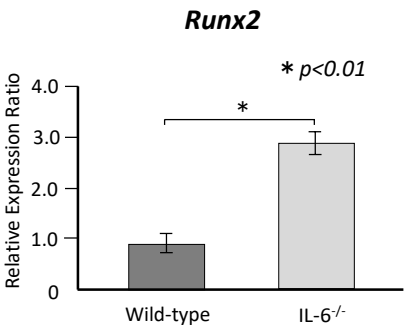
Runx2
Relative Expression Ratio
4.0
3.0
2.0
1.0
0
* p<0.01
*
Wild-type
IL-6-/-

D

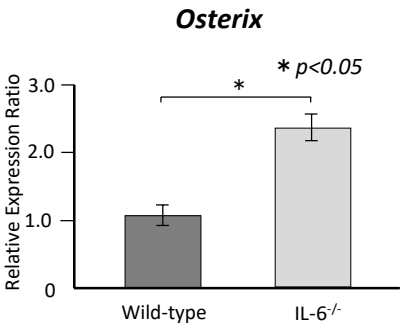
Osterix
Relative Expression Ratio
3.0
2.0
1.0
0
* p<0.05
*
Wild-type
IL-6-/-

E

Fig. 3

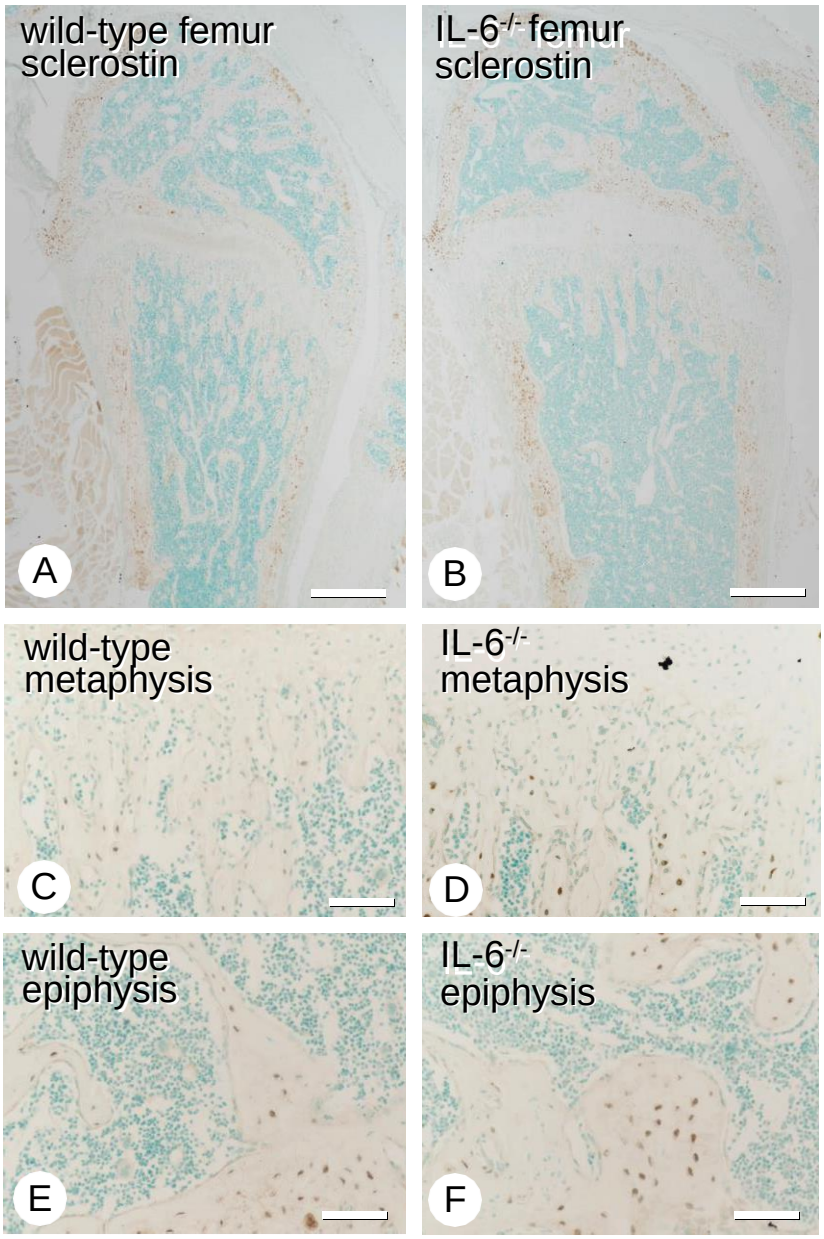
wild-type femur sclerostin
IL-6-/- femur sclerostin
A
B
wild-type metaphysis
IL-6-/- metaphysis
C
D
wild-type epiphysis
IL-6-/- epiphysis
E
F

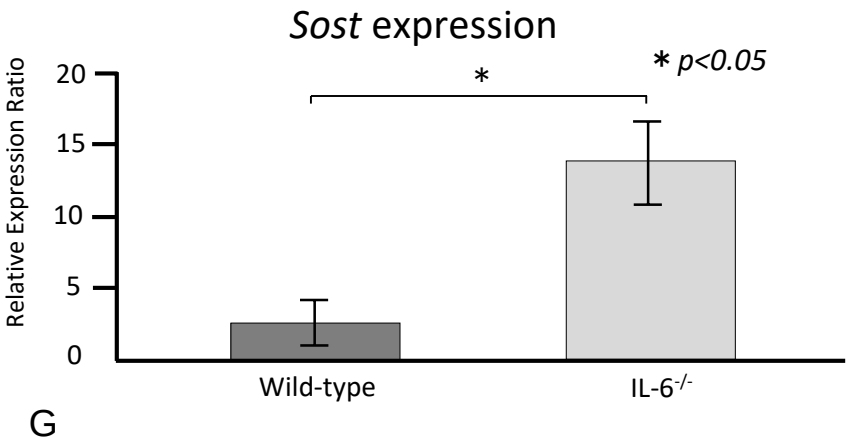
Sost expression
* p<0.05
*
Relative Expression Ratio
20
15
10
5
0
Wild-type
IL-6-/-
G

Fig. 4

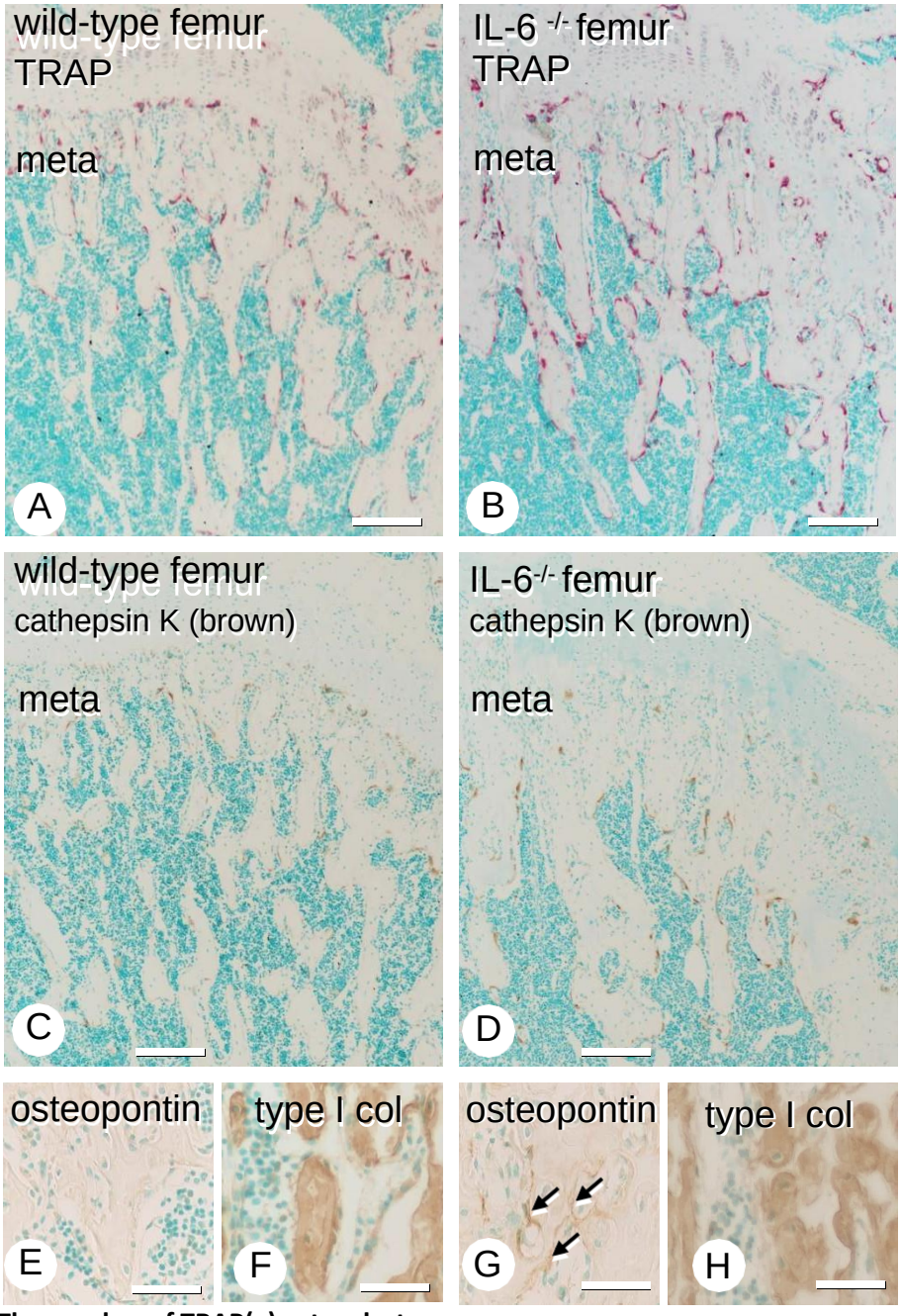
wild-type femur
TRAP
meta
A
IL-6 -/- femur
TRAP
meta
B
wild-type femur
cathepsin K (brown)
meta
C
IL-6-/- femur
cathepsin K (brown)
meta
D
osteopontin
E
type I col
F
osteopontin
G
type I col
H
The number of TRAP(+) osteoclasts
(N)
80
60
40
20
0
*
* p<0.001
Wild-type
IL-6-/-
I
Cathepsin K
Relative Expression Ratio
2.0
1.5
1.0
0.5
0
N.S.
Wild-type
IL-6-/-
J

Fig. 5

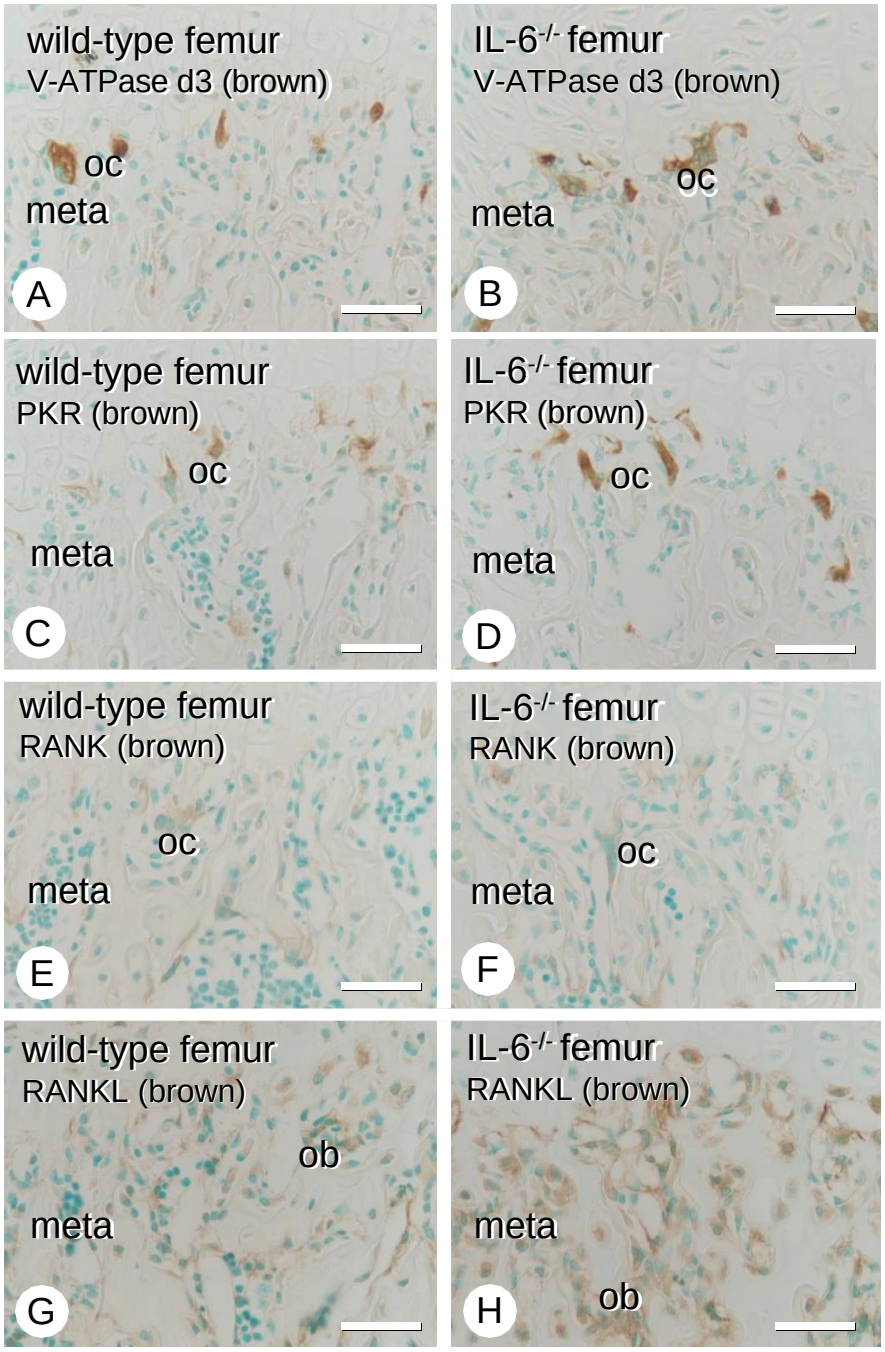
wild-type femur
V-ATPase d3 (brown)
oc
meta
A
IL-6-/- femur
V-ATPase d3 (brown)
oc
meta
B
wild-type femur
PKR (brown)
oc
meta
C
IL-6-/- femur
PKR (brown)
oc
meta
D
wild-type femur
RANK (brown)
oc
meta
E
IL-6-/- femur
RANK (brown)
oc
meta
F
wild-type femur
RANKL (brown)
ob
meta
G
IL-6-/- femur
RANKL (brown)
meta
ob
H

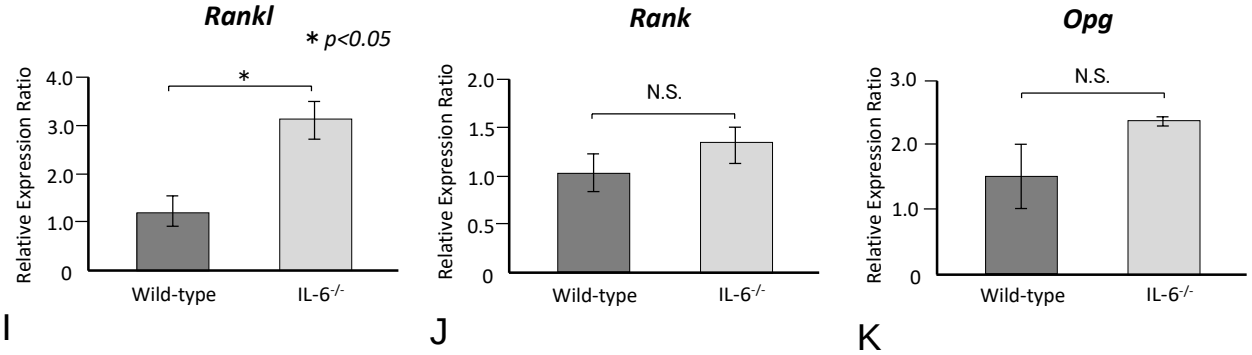
Rankl
* p<0.05
Relative Expression Ratio
4.0
3.0
2.0
1.0
0
*
Wild-type
IL-6-/-
I
Rank
Relative Expression Ratio
2.0
1.5
1.0
0.5
0
N.S.
Wild-type
IL-6-/-
J
Opg
Relative Expression Ratio
3.0
2.0
1.0
0
N.S.
Wild-type
IL-6-/-
K

Fig. 6

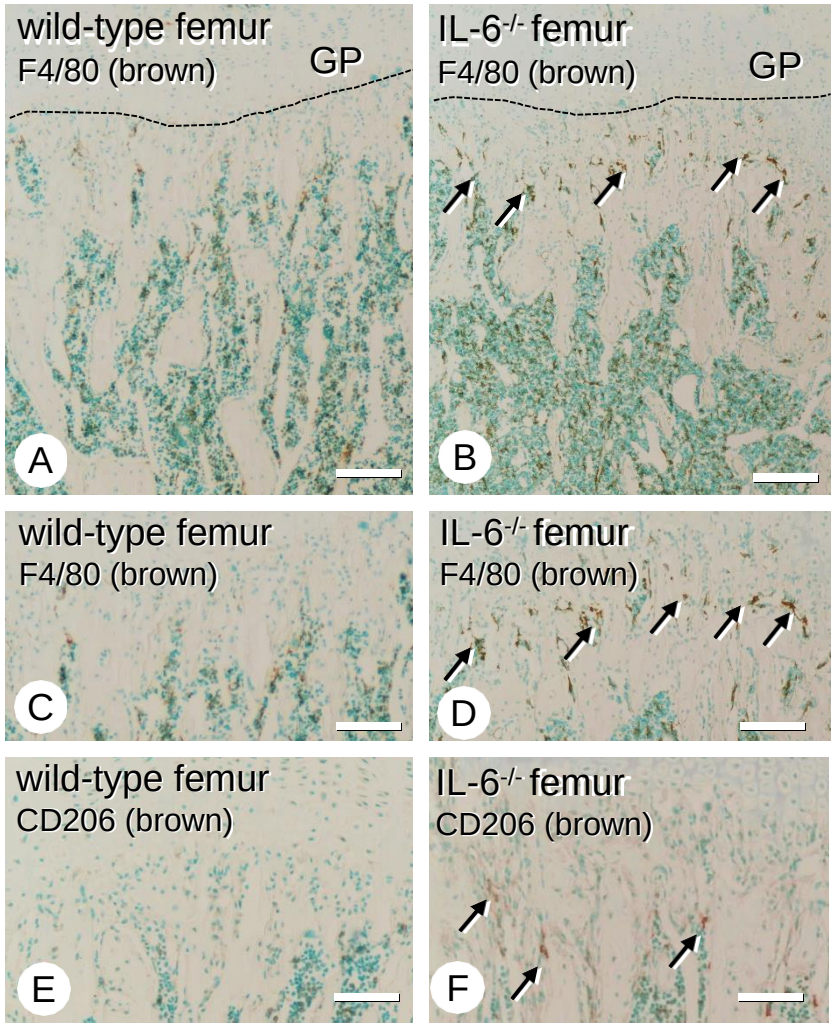
wild-type femur
F4/80 (brown)
GP
A
IL-6-/- femur
F4/80 (brown)
GP
B
wild-type femur
F4/80 (brown)
C
IL-6-/- femur
F4/80 (brown)
D
wild-type femur
CD206 (brown)
E
IL-6-/- femur
CD206 (brown)
F

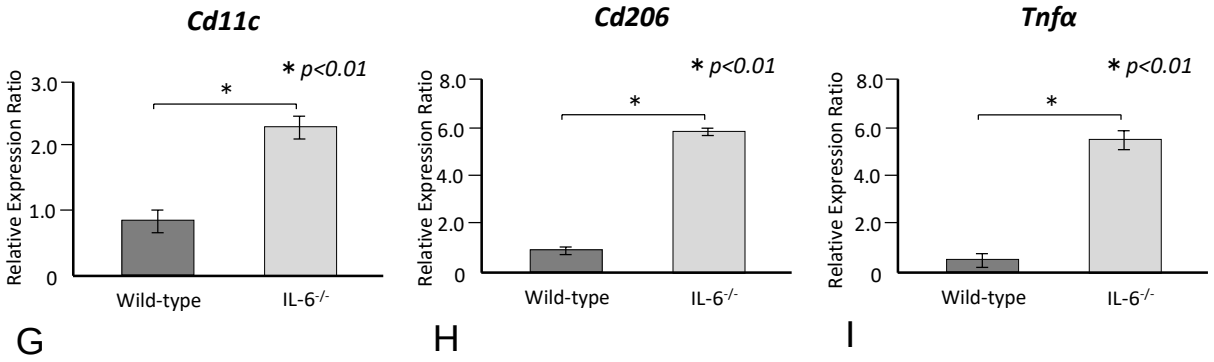
Cd11c
* p<0.01
Relative Expression Ratio
3.0
2.0
1.0
0
Wild-type
IL-6-/-
G
Cd206
* p<0.01
Relative Expression Ratio
8.0
6.0
4.0
2.0
0
Wild-type
IL-6-/-
H
Tnfα
* p<0.01
Relative Expression Ratio
8.0
6.0
4.0
2.0
0
Wild-type
IL-6-/-
I

Fig. 7

Figure legends

Figure 1

Micro CT and histological analyses of the distal extremities of femora of of IL-6$^{-/-}$ mice and wild-type littermates

Micro CT shows less bone volume in the IL-6$^{-/-}$ femoral metaphysis (**B**) compared to the wild-type metaphysis (**A**). Statistical analysis reveals significantly reduced bone mineral density (BMD), but an increased BV/TV in the IL-6$^{-/-}$ femoral metaphysis, compared to the wild-type littermates (See **C** and **D**). IL-6$^{-/-}$ femoral metaphysis histologically demonstrates more metaphyseal trabeculae (**F**), than the wild-type metaphysis (**E**). ob: osteoblast, tb: trabecula

Bars, A, B: 500 μm, **E, F:** 100 μm

Figure 2

Von Kossa Staining of trabeculae and TEM observation of osteoblasts in the metaphyses of wild-type and IL-6$^{-/-}$ femora

Von Kossa staining demonstrates borad mineralized bone matrix (brown color) in the wild-type (**A**) and IL-6$^{-/-}$ metaphyseal trabeculae (**B**). However, the IL-6$^{-/-}$ metaphyseal trabeculae show thick layers of unmineralized bone matrix (blued-colored area, arrows in **D**), while the wild-type trabeculae seem to be completely mineralized (**C**). TEM observation displays the similar ultrastructure of mature osteoblasts in the metaphyses of the wild-type (**E**) and IL-6$^{-/-}$ femora (**F**). ob: osteoblast, tb: trabecula

Bars, A, B: 100 μm, **C, D:** 20 μm, **E, F:** 3 μm

Figure 3

TNALPase(+) area/TV and gene expression of Runx2, Osterix, and Sost in wild-type and IL-6$^{-/-}$ femoral metaphyses

TNALPase immunoreactivity can be seen relatively broad in the metaphyses of IL-6$^{-/-}$ femora (**B**), when compared to the wild-type femora (**A**). Statistical analysis exhibits the increased index of TNALPase(+) area/TV in the IL-6$^{-/-}$ femora, compared with the wild-type counterpart (**C**). Real-time PCR shows the elevated expression of *Runx2* and *Osterix* in the IL-6$^{-/-}$ femora when compared

with the wild-type specimens (**D, E**). ob: osteoblast, tb: trabecula

Bars, A, B: 100 μm

Figure 4

Immunolocalization and geen expression of sclerosrin in the wild-type and IL-6$^{-/-}$ femoral metaphyses

The distribution of sclerostin at low magnified images are not different between wild-type (**A**) and IL-6$^{-/-}$ (**B**) femora. However, when observed at highly-magnified images, sclerostin immunoreactive osteocytes seem to abundant metaphysis (**C, D**) and epiphyses (**E, F**) in the IL-6$^{-/-}$ femora (**D, F**) relative to the wild-type counterparts (**C, E**). Real-time PCR displays markedly increased expression of the *Sost* gene in IL-6$^{-/-}$ femora, when compared with the wild-type femora (**G**)

Bars, A, B: 500 μm, C-F: 100 μm

Figure 5

The distribution of TRAP-positive/cathepsin K-reactive osteoclasts and bone matrix immunopositive for osteopontin and type I collagen in wild-type and IL-6$^{-/-}$ femoral metaphyses

TRAP-positive (**A, B**) / cathepsinK-reactive (**C, D**) osteoclasts can be seen abundant in IL-6$^{-/-}$ femoral metaphysis (**B, D**), rather than in the wild-type metaphysis (**A, C**). There are many osteopontin-positive lines in the IL-6$^{-/-}$ metaphyseal trabeculae (arrows in **G**), though an even but weak immunoreactivity of osteopontin can be seen throughout the wild-type trabeculae (**E**). Unlikely, type I collagen immunoreactivity seems to be uniform in the metaphyseal trabeculae of both the wild-type (**F**) and IL-6$^{-/-}$ metaphyses (**H**). Statistical analysis exhibits the significant increase of the numbers of TRAP-positive osteoclasts in IL-6$^{-/-}$ femoral metaphyses, compared with the wild-type counterpart (**I**). Real-time PCR demonstrates a slightly but not significantly increased expression of *Cathepsin K* in IL-6$^{-/-}$ femora compared with the wild-type counterparts (J). meta: metaphysis

Bars, A, B: 100 μm, **E-H:** 20 μm

Figure 6

Immunolocalization of the d3 subunits of V-ATPase, PKR, RANK and RANKL in the wild-type and IL-6$^{-/-}$ metaphyses

Immunoreactivities (brown color) of V-ATPase (**A, B**), PKR (**C, D**) and RANK (**E, F**) can be observed in osteoclasts in both the wild-type (**A, C, E**) and IL-6$^{-/-}$ femoral metaphyses (**B, D, F**). However, RANKL immunoreactivity (brown color) is seen intense in osteoblasts of IL-6$^{-/-}$ metaphysis (**H**) compared with the wild-type counterpart (**G**). Real-time PCR reveals an increased expression of *Rankl* in the IL-6$^{-/-}$ femora relative to the wild-type femora (**I**). In contrast, there is no significant difference in the expression of *Rank* nor *Opg* between the wild-type and IL-6$^{-/-}$ femora (**J, K**).

Bars A-H: 20 μm

Figure 7

Immunolocalization of F4/80-positive monocytes/macrophages and CD206-reactive cells in the wild-type and IL-6$^{-/-}$ femoral metaphyses

F4/80-positive monocyte/macrophage are localized close to the chondro-osseous junction of the growth plate cartilage (GP) of the IL-6$^{-/-}$ femora (arrows in **B**), when compared with those in the wild-type counterparts (**A**). See the many F4/80-positive brown colored cells (arrows in **D**) close to the growth plate of the IL-6-/- femora (**D**), while F4/80-reactive cells are seen in the region of bone marrow in the wild-type femora (**C**). CD206-immunoreactive cells can be observed in the intertrabecular region of the IL-6$^{-/-}$ metaphysis (arrows in **F**) but not the wild-type specimen (**E**). Real-time PCR demonstrates significantly-enhanced gene expressions of *Cd11c* (G), *Cd206* (H) and *Tnfα* (I) in the IL-6$^{-/-}$ femora when compared with the wild-type specimens**.**

Bars A, B: 100 μm, C-F: 50 μm